ICEMS
Hangzhou 2014

The 17th International Conference on Electrical Machines and Systems

ICEMS 2014

Hangzhou, China, October 22-25, 2014

Welcome Message

Committees

Keynote Speeches

Invited Speeches

Industry Technical Sessions

Technical Sessions

Author Index

Supporters and Exhibitors

LS6F 2   Optimal Design of a Linear Induction Motor for Woodworking Machine Application
Shuai Wang, Dong-Min Miao, and Jian-Xin Shen
Zhejiang University, China

LS6F 3   Analysis of Coupling Effect of Double-side Linear Induction Motor with Shielding Structure
Yuxing Zhang, Chengmei Lin, Jin Xu, and Zhaolong Sun
Naval University of Engineering, China

LS6F 4   Magnet Arrangement of Linear PM Vernier Machine
Takayuki Imada, and Shoji Shimomura
Shibaura Institute of Technology, Japan

LS6F 5   A New Modular and Complementary Double-Sided Linear Flux-Switching Permanent Magnet Motor with Yokeless Secondary
Ruiwu Cao[1], Wenxin Huang[1], and Ming Cheng[2]
[1]Nanjing University of Aeronautics and Astronautics, China, [2]Southeast University, China

LS6F 6   Dynamic MEC Modeling of a Linear Tubular PM Machine
Mohamed Wael Zouaghi, Amal Souissi, Imen Abdennadher, and Ahmed Masmoudi
University of Sfax, Tunisia

ICEMS2014 Poster Presentation Schedule

DS1H1   PM Motor Drives 1

DS1H1-1   Influence of Magnet Layer Number on Electromagnetic Performance of Interior Ferrite Permanent Magnet Synchronous Machine
Weizhong Fei, Wenyi Liang, and Patrick Chi-Kwong Luk
Cranfield University, UK

DS1H1-2   Analysis and Determination of Mechanical Bearing Load Caused by Unbalanced Magnetic Pull
Andreas Ruf, Michael Schröder, Aryanti Putri, David Franck, and Kay Hameyer
RWTH Aachen University, Germany

ICEMS
Hangzhou 2014

Analysis and determination of mechanical bearing load caused by unbalanced magnetic pull

Andreas Ruf, Michael Schröder, Aryanti Putri, David Franck, Kay Hameyer

Institute of Electrical Machines

RWTH Aachen University

Aachen 52062, Germany

Email: Andreas.Ruf@iem.rwth-aachen.de

Abstract—One common mechanical fault in electrical drives applied to industrial processes are related to bearing damage [1]. These faults can be brought forward by mechanical and thermal stress during the operation. This paper focuses on the radial electromagnetic forces, which are known as static and dynamic unbalanced magnetic pull (UMP), caused by rotor eccentricities. In particular in this paper the interaction of the rotor position and the amplitude of the static and dynamic eccentricity, the slot harmonics and saturation effects in the entire operational range of a permanent magnet synchronous machine (PMSM) are studied.

I. INTRODUCTION

Electrical drives in industrial applications are manufactured by mass production. Hence, deviations caused by the production such as displacements of the bearing seats, uneven rotor magnetization [2], or displacements of the rotational axis of the rotor are unavoidable as described in [3], [4] and [5]. Amongst others, this leads to a rotor eccentricity and causes an unbalanced magnetic pull, which mechanically burdens the bearings. One widely applied approach to estimate this additional stress on the bearings is an electromagnetic worst case simulation of a particular operating point. In this paper the UMP in the complete operational region is studied in order to have a more sophisticated base for the approximation of the occurring forces.

II. THEORY

The magnetic flux density in the airgap of an electrical machine

$$B(\alpha, t) = \Theta(\alpha, t) \cdot \Lambda(\alpha, t) \qquad (1)$$

is calculated from the magnetomotive force $\Theta(\alpha, t)$ and the magnetic permeance $\Lambda(\alpha, t)$, where α is an angular position in the airgap of the machine and t is a moment in time. For an uniform airgap the permeance can be simply described by

$$\Lambda = \frac{\mu_0}{\delta_m}, \qquad (2)$$

with the vacuum permeability μ_0 and the uniform airgap length δ_m [6]. Due to slotting of stator or rotor, static or dynamic eccentricities, or saturation of the magnetic materials in the electrical machine, the airgap can not be assumed as constant.

To consider these effects, the simple magnetic permeance from equation 2 is multiplied by specific permeances λ:

$$\Lambda(\alpha, t) = \frac{\mu_0}{\delta_m} \cdot \lambda_S \cdot \lambda_R \cdot \lambda_{SE} \cdot \lambda_{DE} \cdot \lambda_{sat}. \qquad (3)$$

Stator and rotor slotting as well as saturation are considered by the specific permeances λ_S, λ_R and λ_{sat} respectively and can be determined as described in [6] and [7].

Eccentricity occurs in rotating machines when the stator center is not in the same position as the rotor's center. Figure 1 schematically illustrates an eccentric machine with the stator center M, the stator inner radius R, the rotor center S and the rotor radius r. The displacement between M and S is the eccentricity $e = \overline{MS}$ of the machine.
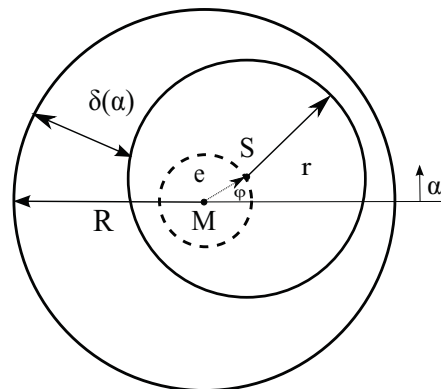

Fig. 1: Mathematical model for the airgap calculation of an eccentric rotating machine.

Depending on the position of the rotating axis the eccentricity is dynamic or static. For the case, that the rotation axis is at the position of the rotor center S the eccentricity is called static eccentricity and the position of the smallest airgap length remains at one location around the circumference. For the other case, if the rotation axis is at the position of the stator center M, the center of the rotor rotates on the dashed circle. The eccentric motion is called dynamic eccentricity and the position of the smallest airgap revolves. In general, both types of eccentricity may occur at the same time and lead to a mixed eccentricity.

8

With the average airgap length $\delta_\mathrm{m} = R - r$ the relative eccentricity ϵ can be expressed as

$$\epsilon = \frac{e}{R-r} = \frac{e}{\delta_\mathrm{m}}. \tag{4}$$

For practically relevant eccentricities $\delta_\mathrm{m} \ll R$, the airgap length $\delta(\alpha)$ can be determined for the case of static eccentricity as

$$\delta(\alpha) = \delta_\mathrm{m} \cdot \left(1 - \epsilon \cdot \cos(\alpha - \varphi)\right), \tag{5}$$

where α is the angular position in the airgap and φ the angle of the eccentricity.

For the case of dynamic eccentricity, the airgap length $\delta(\alpha, t)$ becomes dependent on time:

$$\delta(\alpha, t) = \delta_\mathrm{m} \cdot \left(1 - \epsilon \cdot \cos(\alpha - \omega t - \varphi)\right), \tag{6}$$

where ω is the angular frequency of the rotor.

Using this equations for the airgap length, static and dynamic eccentricity can be considered for the magnetic permeance as shown in [8] by using the following simplified specific permeances:

$$\lambda_\mathrm{SE}(\alpha) \approx \frac{1}{\sqrt{1+\epsilon^2}} + 2 \cdot \frac{1 - \sqrt{1-\epsilon^2}}{\epsilon \cdot \sqrt{1-\epsilon^2}} \cdot \cos(\alpha) \ \text{and} \tag{7}$$

$$\lambda_\mathrm{DE}(\alpha, t) \approx \frac{1}{\sqrt{1+\epsilon^2}} + 2 \cdot \frac{1 - \sqrt{1-\epsilon^2}}{\epsilon \cdot \sqrt{1-\epsilon^2}} \cdot \cos(\omega t - \alpha). \tag{8}$$

The magnetic flux density in the airgap of an electrical machine from equation 1 is a vector quantity and can be divided into its two components $B_\mathrm{rad}(\alpha, t)$ and $B_\mathrm{tan}(\alpha, t)$ – the radial and tangential component. The force density at the intersection between the machine's airgap and the stator can be derived from the LORENTZ force and simplified by means of the MAXWELL stress tensor. This results in the well-known equations for the tangential component of the force density

$$\sigma_\mathrm{tan}(\alpha, t) = \frac{1}{\mu_0} \cdot B_\mathrm{rad}(\alpha, t) \cdot B_\mathrm{tan}(\alpha, t) \tag{9}$$

and the radial component [9]

$$\begin{aligned}
\sigma_\mathrm{rad}(\alpha, t) &= \frac{1}{2\mu_0} \cdot \left(B_\mathrm{rad}^2(\alpha, t) - B_\mathrm{tan}^2(\alpha, t)\right) \\
&\approx \frac{1}{2\mu_0} \cdot B_\mathrm{rad}^2(\alpha, t).
\end{aligned} \tag{10}$$

The magnetic permeability μ of the ferromagnetic material is much higher than that of the airgap (e. g. $\mu_\mathrm{Fe} \approx 10000 \gg \mu_\mathrm{Air} \approx 1$). For this reason the magnetic flux lines run predominantly in radial direction through the airgap, so that the radial flux density $B_\mathrm{rad}(\alpha, t)$ is much higher than the tangential one $B_\mathrm{tan}(\alpha, t)$. This results in the simplified approximation in equation 10 [8]. The tangential force density σ_tan is necessary for the torque production in the electrical machine. The integral over the tangential force density along the airgap in circumferential direction yields the mechanical torque T. The radial force density σ_rad acts on the stator teeth and deforms the stator. It is the main cause of vibration and noise from

electrical machines and in case of eccentricities it causes the unbalanced magnetic pull.

The radial forces can be calculated through the integral over the radial force density along the airgap in circumferential direction:

$$F_\mathrm{rad}(t) = R \cdot l \cdot \int_0^{2\pi} \sigma_\mathrm{rad}(\alpha, t) \, \mathrm{d}\alpha, \tag{11}$$

where l is the length of the machine in axial direction.

III. CALCULATION OF OPERATING POINTS

The following section introduces a methodology to incorporate the operation characteristics in the simulation of electrical machines. In order to evaluate the proposed methodology a PMSM with buried magnets in the rotor is studied [10].
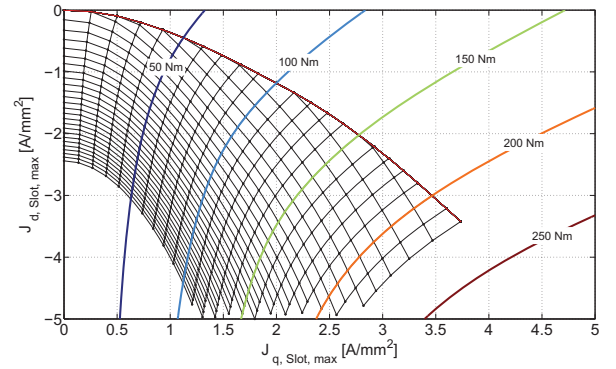

Fig. 2: Simulated map of the average torque in Nm with overlaid mesh of operating points.

The electrical machine is modeled in a rotor-flux-fixed dq-reference frame including cross coupling magnetization and saturation [11]:

$$\begin{bmatrix} \hat{\Psi}_\mathrm{d} \\ \hat{\Psi}_\mathrm{q} \end{bmatrix} = \begin{bmatrix} L_\mathrm{dd} & L_\mathrm{dq} \\ L_\mathrm{qd} & L_\mathrm{qq} \end{bmatrix} \begin{bmatrix} \hat{i}_\mathrm{d} \\ \hat{i}_\mathrm{q} \end{bmatrix} + \begin{bmatrix} \hat{\Psi}_\mathrm{f,d} \\ \hat{\Psi}_\mathrm{f,q} \end{bmatrix}. \tag{12}$$

The quadrature and direct current is varied during the simulation to extract the average torque determined by the eggshell method [12] for different excitations. The flux-linkage vector is calculated with the geometrical summation:

$$\hat{\Psi} = \sqrt{\hat{\Psi}_\mathrm{d}^2 + \hat{\Psi}_\mathrm{q}^2}. \tag{13}$$

In order to calculate the operating points for the whole operating range a combined control strategy is used. The optimization problem is defined by:

$$\begin{aligned}
\underset{\hat{i}_{d,i,j}, \hat{i}_{q,i,j} \in \mathbb{R}}{\text{minimize}} \quad & \mathrm{J}(\hat{i}_{d,i,j}, \hat{i}_{q,i,j}) = \sqrt{\hat{i}_{d,i,j}^2 + \hat{i}_{q,i,j}^2} \\
\text{subject to} \quad & T_i = \frac{3}{2} p \left(\hat{\Psi}_{d,i}\hat{i}_{q,i} - \hat{\Psi}_{q,i}\hat{i}_{d,i}\right), \quad \forall\, i = 1, \ldots, m, \\
& \hat{u}_j = \omega_j \hat{\Psi}_{d,i} \leq \hat{u}_{max}, \quad\quad\quad \forall\, j = 1, \ldots, n,
\end{aligned}$$

with the torque vector $T_1, T_2, ..., T_m$ subject to $m \in \mathbb{N}$ and the speed vector $n_1, n_2, ..., n_\mathrm{n}$ with $n \in \mathbb{N}$. This optimization

problem combines the maximum torque per ampere (MTPA) control for the base speed range and the maximum torque per voltage (MTPV) control for the field weakening range [13].

Figure 2 shows the trajectories of the average electromagnetic torque calculated with different current excitations. Further an overlaid mesh of calculated operating points ($f_{el} = 0\,Hz - 400\,Hz$, $T_{el} = 0\,Nm - 220\,Nm$), using the combined control strategy, is mapped. The rotor-flux-oriented current vectors are defined by the operating points, which are calculated for the given optimization problem. The basic speed range is represented by the trajectory that extends along the rising torques (MTPA-line), whereas the field weakening area is represented by the mesh below this trajectory.

Figures 3 and 4 illustrate the direct und quadrature current component speed-torque map for the entire operating range for a maximum amplitude of the induced voltage of $\hat{u} = 360\,V$. This defined dq-current combinations are used to calculate for each operating point the UMP in the entire operating range of the PMSM.
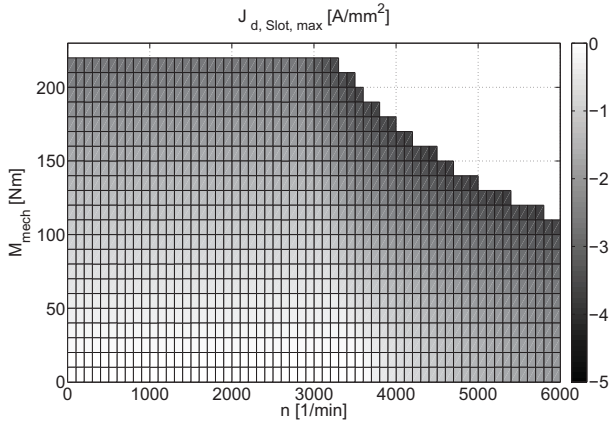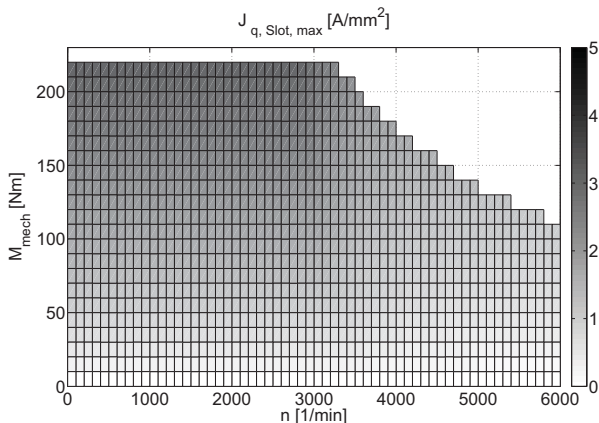

Fig. 3: Direct current densitiy per slot.

Fig. 4: Quadrature current density per slot.

IV. CALCULATION OF THE UNBALANCED MAGNETIC PULL

In order to evaluate the influence of dynamic and static eccentricity on the behavior of the UMP, different positions

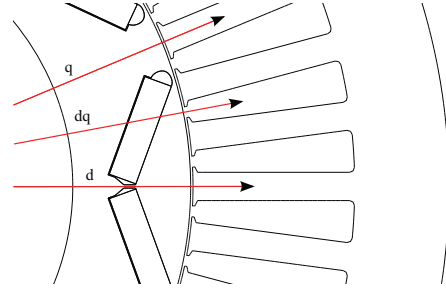of the smallest airgap of the eccentricity vector are modeled (Figure 5 and Figure 6).

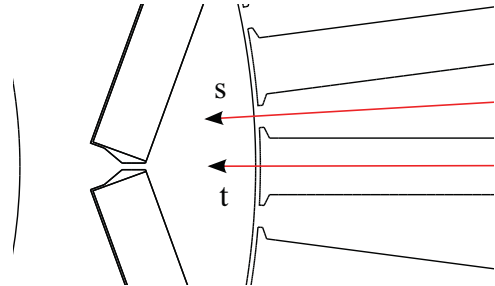Fig. 5: Simulated positions of dynamic rotor eccentricity.

Fig. 6: Simulated positions of static rotor eccentricity.

To consider effects of slotting and saturation, a finite element (FE) model is employed.

To determine the forces caused by eccentricity on the machine's behavior the Eggshell method [12] is employed. Figure 7 illustrates the result of the computation of the electromagnetic forces on the circumference of the rotor:
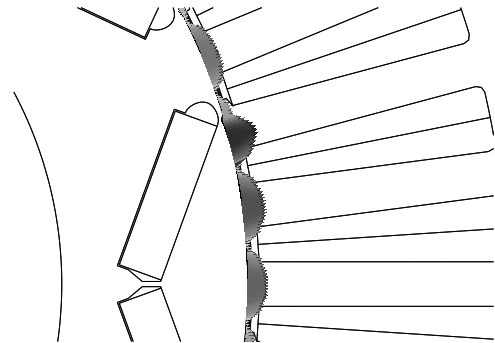

Fig. 7: Electromagnetic forces on the cirumference of the rotor.

These forces are decomposed into a tangential and a radial component. The radial component of these electromagnetic forces are presented in Figure 8. The radial force consists of the slot harmonics with $N = 48$, the order of the poles $2p = 8$ and the harmonic order caused by the variing permeance through the eccentricity $N_{ex} = 1$. The radial forces are integrated along the circumference of the rotor in order to calculate the unbalanced magnetic pull. This is done for each position of the rotor at rotor-fixed-coordinate frame
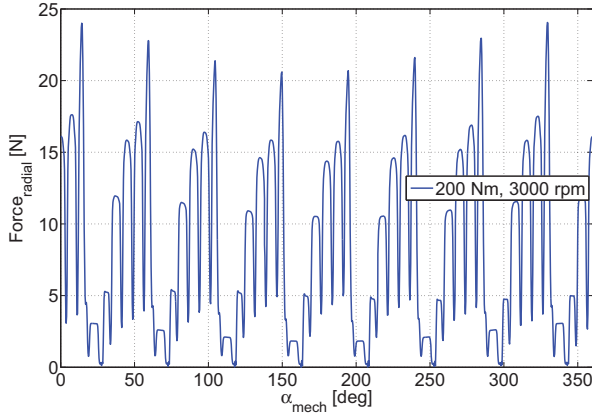
Fig. 8: Radial component of the electromagnetic forces versus the angle along the cirumference ($\epsilon = 2/7$).

for dynamic eccentricity and stator-fixed-coordinate frame for static eccentricity. The rotation-angle-dependent behavior of the UMP will be thereafter evaluated. The presented operating points in section 3 are used to calculate the UMP for different current excitations in the entire operational range of the used PMSM. To study the influence of the eccentricity angle of the rotor, the positions of the eccentricity are varied according to Figure 5 and 6.

V. RESULTS

A. Dynamic eccentricity

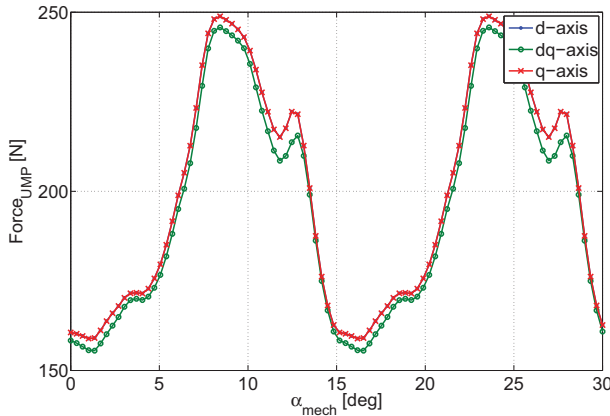The influence of the position of the eccentricity vector is presented in Figure 9.

Fig. 9: UMP versus the mechanical angle for different positions of the eccentricity vector.

From Figure 9 can be concluded that the position of the eccentricity has a not significant influence to the UMP. The UMPs caused by the displacements in d- and q-axis are identical and between the axes is only slightly lower than the first. The amplitude and the harmonics are effected by the specific permeance of the rotor λ_R. In case of a PMSM

with buried permanent magnets, the rotor has no slots and the specific permeance is only influenced by the geometry of the rotor. As illustrated in Figure 9, the specific permeance of the rotor has a minor effect when compared to the slot harmonics of the stator.
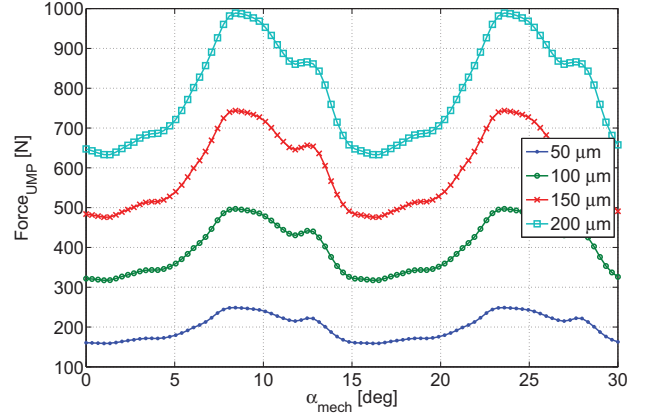

Fig. 10: UMP as a function of the mechanical angle for different amplitudes of the eccentricity vector ($\delta_m = 700\,\mu m$).

In Figure 10 the effects of rising amplitude of the eccentricity vector on the amplitude of UMP are illustrated. The increase in the eccentricity effects an nearly linear increase of the average and all harmonics of the UMP in the range of practically occurring eccentricity amplitudes (Figure 11).
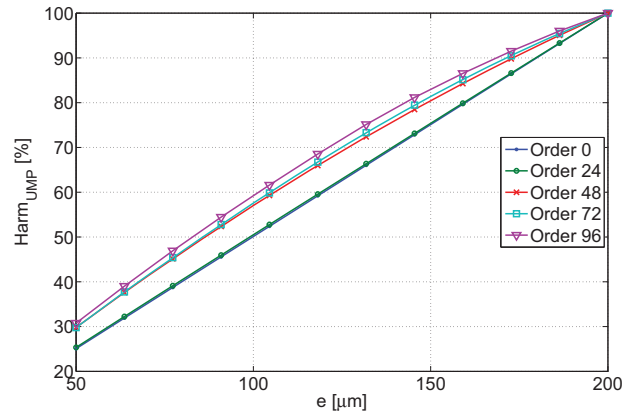

Fig. 11: Harmonics of the UMP as a function of the amplitude of the eccentricity vector ($\delta_m = 700\,\mu m$).

A tolerance analysis of the electrical machine used in the simulation has revealed that the most likely eccentricity is in the range of $e = 50\,\mu m$ i.e. $\epsilon = 1/14$ ($\delta_m = 700\,\mu m$). For this reason, the following results are presented for this amplitude of the eccentricity vector in order to make the results more comprehensible.

Figure 12 shows the calculated average UMP and the operating points for different current excitations. It is apparent that the UMP depends on the position of the flux linkage,
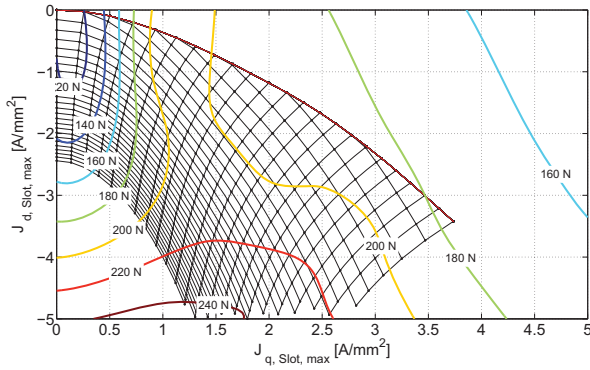
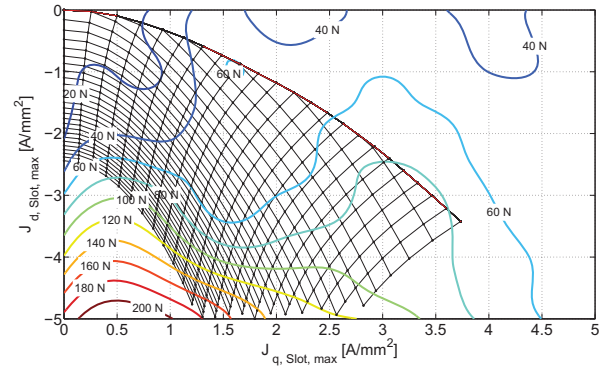Fig. 12: Simulated map of the average UMP in N with overlaid mesh of operating points.

Fig. 14: Simulated map of the harmonic component of the UMP in N with overlaid mesh of operating points.
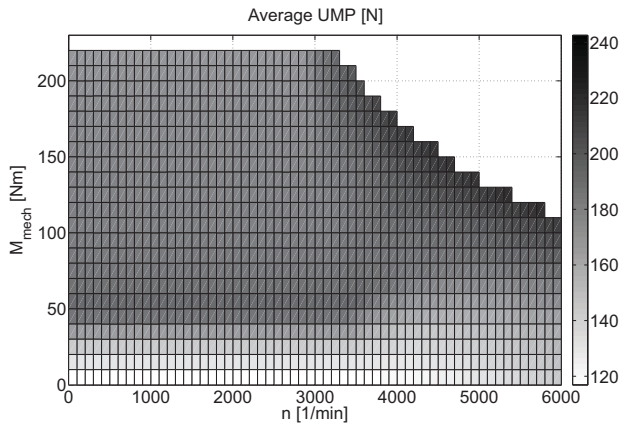

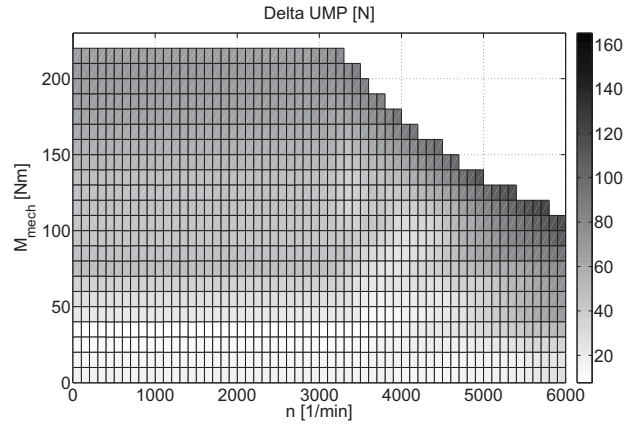Fig. 13: Speed-torque map of the average UMP.

Fig. 15: Simulated map of the average torque in Nm with overlaid mesh of operating points.

relative to the position of the eccentricity vector. Starting from the no-load point, the average of the UMP increases with the increase of the quadrature current and the negative direct current. Depending on the quadrature current the average UMP reaches its maximum, while depending on the direct current the UMP increases continuously.

Figure 13 illustrates the average UMP in the speed-torque map. The maximum of the average UMP depending on the quadrature current can also been seen in base speed range of the machine at 55 Nm. In the field weakening range the quadrature current decreases for a given torque and the direct current increases. This effects an increase of the UMP up to the maximum for the whole speed-torque map.

The results for the harmonic component of the UMP are presented in Figure 14. The harmonic component is a distinctive proportion of the UMP and increases in direction of increasing quadrature current and direct current. However the increase depending on the direct current dominates also for the harmonic component. In the speed-torque map of the harmonic component (Figure 15) has also its maximum at high frequencys and high torques. In the base speed range the harmonic component increases with the increase of torque almost continuously. In the area of low torque the harmonic

component is modest.

Figure 16 presents the behavior of the UMP as a function of the rotation angle of the rotor for two chosen operating points: at nominal point $(3.000\,\mathrm{rpm},\ T = 200\,\mathrm{Nm})$ and at maximum flux weakening point $(6.000\,\mathrm{rpm},\ T = 100\,\mathrm{Nm})$. The UMP
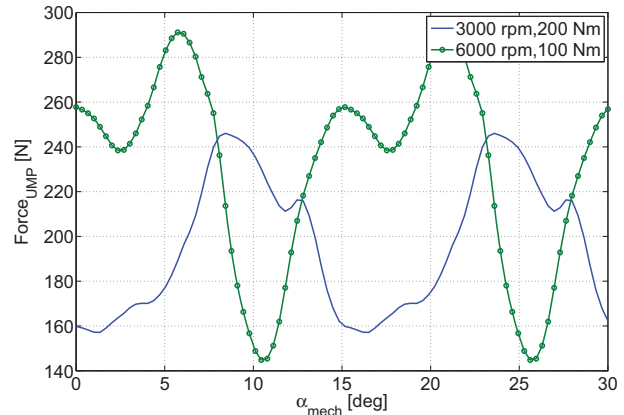

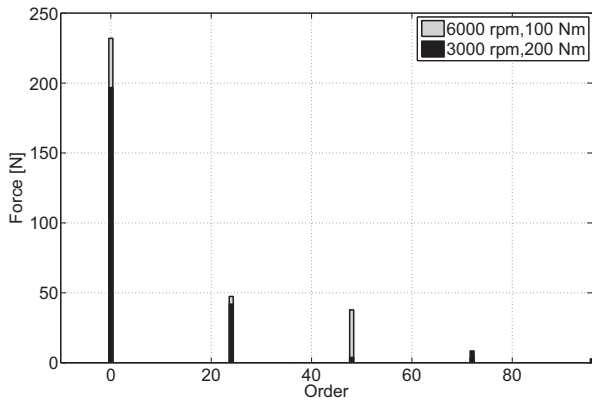Fig. 16: UMP versus the mechanical angle for two different operating points.

Fig. 17: Fast fourier transformation of UMP for two different operating points.
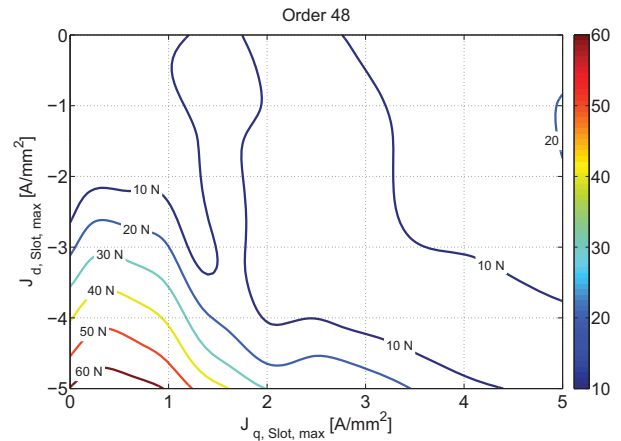
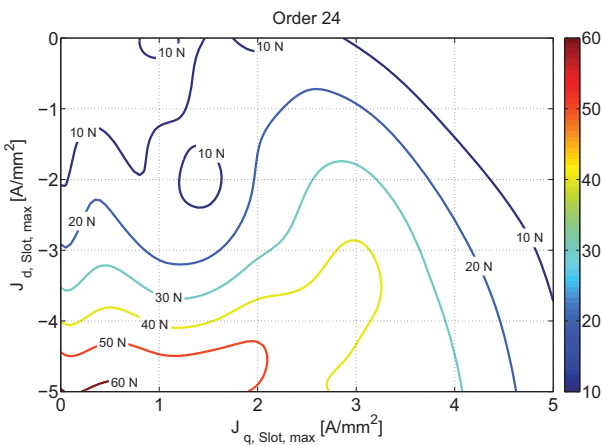

Fig. 19: Simulated map of harmonic component 48.

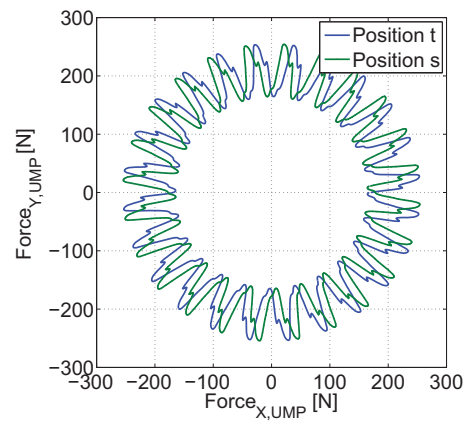Fig. 18: Simulated map of harmonic component 24.

Fig. 20: UMP caused by static eccentricity in rotor fixed reference frame for position t and s ($50\,\mu\text{m}$).

at 6.000 rpm has a higher harmonic and average component than the UMP at 3.000 rpm. The harmonic components of both operating points calculated with FFT, are shown in Figure 17. The UMP harmonics for the operating point at maximum flux weakening are generally higher than at the nominal operating point. This is caused by the higher proportion of direct current, which leads to a higher UMP, as shown in Figure 13 and 15. The order 24 and 48 are the dominant harmonics for both operating points. The order 48 is caused by the stator slotting and the harmonic component 24 by saturation.

The dependencies of these harmonic components are shown in Figure 18 and 19. Both components are increasing with the increase of the direct current. The order 24 is also dependent on the quadrature current, while the order 48 caused by stator slots is almost independent of the quadrature current.

B. Static eccentricity

The calculation of the static eccentricity is analogous to the method described for the dynamic eccentricity. The UMP is calculated by integration of the radial force density on the circumference of the rotor.

Figure 20 presents the UMP caused by static eccentricity in rotor-fixed frame, calculated for the nominal point (3.000 rpm, $T = 200\,\text{Nm}$). The UMP acts in the direction of the smallest air gap. This position of the air gap rotates from the perspective of the rotor, and therefore the UMP is also rotating. The difference in the position of the static eccentricity only influences the angular position of the UMP. For both cases the order 24 and 48 are dominant, caused as described by stator slotting and saturation. In order to describe the behavior on the time domain, the UMP is transformed to the point of smallest air gap in the stator-fixed frame.

Comparing the results presented in Figure 12 and 14 for the dynamic eccentricity, the stator currents are varied for the same eccentricity amplitude $e = 50\,\mu\text{m}$ e.g. $\epsilon = 1/14$ and decomposed into an average and harmonic component. The result are illustrated in Figure 21 and 22.

It can be seen that the results differ in a negligible extent. An examination of the harmonics distribution give the same result as shown in Figure 18 and 19.
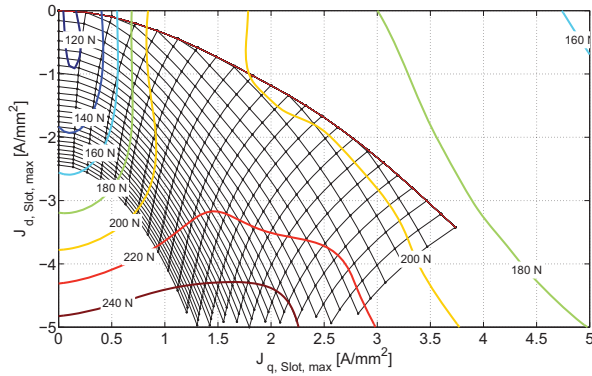
13

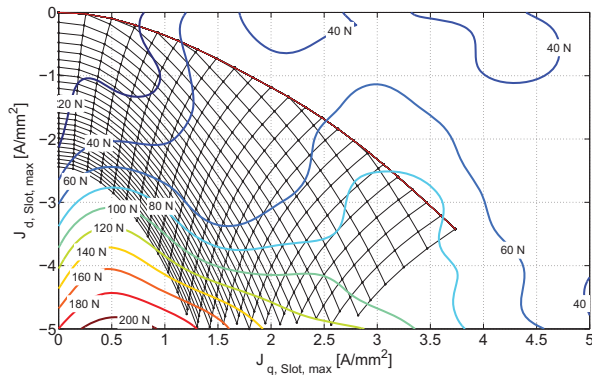Fig. 21: Simulated map of the average UMP in N with overlaid mesh of operating points (static eccentricity).

Fig. 22: Simulated map of the harmonic component of the UMP in N with overlaid mesh of operating points (static eccentricity).

VI. Conclusion

In this paper a methodology to study the influence of the position and the amplitude of the eccentricity for the whole operational range of PMSM is discussed. It has been shown that the position of the eccentricity has a not significant influence on the behaviour of the UMP and is therefore neglected. The amplitude of the eccentricity vector influences the amplitude of the UMP including all harmonic force components. For technical relevant eccentricities, the influence is approximately linear for the average and the dominant harmonics of the UMP. In most cases it is sufficient to displace the rotor at an arbitrary position and amplitude. Local force distribution due to static and dynamic eccentricity reveal the same circumference but differ in their frequency components. When applying the stator fixed reference frame in case of a static eccentricity and a rotor fixed reference frame in case of dynamic eccentricity both types of eccentricity show the same characteristics. Therefore a transformation from static to dynamic eccentricity in the simulations and vice versa is valid.

In conclusion it is suffcient to simulate one type of eccentricity (static or dynamic) with an arbitrary value of displacement (rotor or stator) to evaluate all possible airgap unbalances. When varying the current excitation the UMP for all possible operation points and all possible eccentricities can be calculated with a reduced computational effort when compared to classical computation methods. This allows for the application of the proposed model in stochastic simulations and enables an a priori design and lifetime estimation of bearings.

References

[1] A. Bonnett and C. Yung, "Increased efficiency versus increased reliability," *Industry Applications Magazine, IEEE*, vol. 14, no. 1, pp. 29–36, Jan 2008.

[2] M. Novak and M. Kosek, "Unbalanced magnetic pull induced by the uneven rotor magnetization of permanent magnet synchronous motor," in *ELEKTRO, 2014*, May 2014, pp. 347–351.

[3] A. Smith and D. Dorrell, "Calculation and measurement of unbalanced magnetic pull in cage induction motors with eccentric rotors. i. analytical model," *Electric Power Applications, IEE Proceedings -*, vol. 143, no. 3, pp. 193–201, May 1996.

[4] P. Frauman, A. Burakov, and A. Arkkio, "Effects of the slot harmonics on the unbalanced magnetic pull in an induction motor with an eccentric rotor," *Magnetics, IEEE Transactions on*, vol. 43, no. 8, pp. 3441–3444, Aug 2007.

[5] D. Dorrell, A. Hermann, and B. Jensen, "Analysis of unbalanced magnetic pull in wound rotor induction machines using finite element analysis - transient, motoring and generating modes," in *Industrial Electronics Society, IECON 2013 - 39th Annual Conference of the IEEE*, Nov 2013, pp. 7307–7312.

[6] H. O. Seinsch, *Oberfelderscheinungen in Drehfeldmaschinen – Grundlagen zur analytischen und numerischen Berechnung*. Stuttgart: Teubner, 1992.

[7] K. Oberretl, "Losses, torques and magnetic noise in induction motors with static converter supply, taking multiple armature reaction and slot openings into account," *Electric Power Applications, IET*, vol. 1, no. 4, pp. 517–531, July 2007.

[8] J. F. Gieras, C. Wang, and J. Cho Lai, *Noise of Polyphase Electric Motors*. USA: CRC Press (Taylor & Francis Group), 2006.

[9] A. Smith and D. Dorrell, "Calculation and measurement of unbalanced magnetic pull in cage induction motors with eccentric rotors. i. analytical model," *Electric Power Applications, IEE Proceedings -*, vol. 143, no. 3, pp. 193–201, May 1996.

[10] T. Finken, M. Hombitzer, and K. Hameyer, "Study and comparison of several permanent-magnet excited rotor types regarding their applicability in electric vehicles," in *Emobility - Electrical Power Train, 2010*, Nov 2010, pp. 1–7.

[11] T. Herold, D. Franck, E. Lange, and K. Hameyer, "Extension of a D-Q Model of a Permanent Magnet Excited Synchronous Machine by Including Saturation, Cross-Coupling and Slotting Effects," in *International Electric Machines and Drives Conference, IEMDC 2011*. Professor M. A. Rahman, Canada, 2011.

[12] F. Henrotte, G. Deliége, and K. Hameyer, "The eggshell approach for the computation of electromagnetic forces in 2d and 3d," *COMPEL*, vol. 23, no. 4, pp. 996–1005, 2004.

[13] R. De Doncker, D. Pulle, and A. Veltman, *Advanced Electrical Drives: Analysis, Modeling, Control*. Springer, 2010.